Theoretical proof of parameter optimization for sinusoidal fringe projection profilometry☆

Tao Yang [a], Guanliang Zhang [a], Huanhuan Li [a], Zhongzhi Zhang [a], Xiang Zhou [a,b,*]

[a] School of Mechanical Engineering, Xi'an Jiaotong University, Xi'an, Shaanxi 710049, China
[b] School of Food Equipment Engineering and Science, Xi'an Jiaotong University, Xi'an, Shaanxi 710049, China

ARTICLE INFO

ABSTRACT

In sinusoidal fringe projection profilometry (FPP), many factors are known to improve measurement accuracy. However, the parameters of the projected fringe pattern, such as modulation and pitch, are the most basic factors. Some empirical principles have been described by researchers, but there is still a lack of theoretical support. In this study, we attempt to address this problem by providing a theoretical proof. We first build an error model for the FPP system. The model reveals how the pitch, modulation, and noise of the fringe pattern affect the measurement error. Combined with optical projection analysis, an optimal projection pitch is delivered that yields the best performance. Both simulations and experiments verify the proposed theoretical proof and optimization method, which will facilitate the construction of FPP systems and help users avoid empiricism and time-consuming experiments.

1. Introduction

Sinusoidal fringe projection profilometry (FPP) is one of the most popular non-contact methods for analyzing the surfaces of three-dimensional (3D) objects. It has been implemented extensively in applications including industrial monitoring, computer vision, virtual reality, and biomedicine providing the advantages of high precision, high resolution, full field, and easy implementation [1,2].

There are many factors that can significantly affect the performance of FPP. Researchers are always exploring new ways to improve the FPP system by analyzing and optimizing these factors. When using a digital device to project fringe patterns, nonlinearity, which makes ideal sinusoidal waveforms non-sinusoidal, is inevitable. To overcome this problem, Liu et al. built a mathematical gamma model to predict its effects on FPP [3]. Meanwhile, Zhang and Huang [4] proposed a widely used lookup table approach to compensate for the phase error directly, without employing any mathematical models. Some other methods based on statistical analysis [5], Fourier spectrum analysis [6], and polynomial fitting [6] have been proposed to correct gamma distortion. Considering the bidirectional reflectance distribution function (BRDF) of the measuring surface, some researchers adjust the pixel-wise intensity of the projected fringe patterns, which is feedback with the captured texture, to adapt to highly dynamic surfaces [7,8]. A phase-shifting method [1,9] is usually used to recover the highly accurate phase. Experiments by Jia

et al. have shown that higher measurement accuracy can be achieved by using a greater number of phase-shifting steps [10] and a similar phenomenon is shown in experiments by Cai et al. [11]. However, when the phase-shifting steps are above a threshold (7 is suggested in [2]), there is no significant reduction in the measurement error, which was also verified by Zhang et al.'s experiments [12,13]. Lei and Zhang's research has revealed the relationship between the phase error and the focusing level of sinusoidal patterns [14]. They found that focusing sinusoidal patterns have a better performance than defocusing sinusoidal patterns and that defocused binary fringe patterns can achieve similar performance to sinusoidal patterns with the same defocus level. Other researchers have tried to optimize the FPP system by changing the direction of the fringe pattern. Wang and Zhang [15] demonstrated that horizontal and vertical fringe patterns are not usually optimal when the phase change is the largest at a given depth variation. They projected a set of horizontal and vertical fringe patterns onto a step-height object and found the optimal direction by analyzing two resultant phase maps. Zhang et al. suggested that the optimal fringes are circular-arc-shaped and centered at the episode, giving the best phase sensitivities over the whole fringe pattern [16]. Zhang et al. published state-of-the-art results in [12], in which the background of the fringe pattern also has a nonlinear effect on the phase error. A lower background means that there will be a lower-quality fringe pattern resulting in a larger phase error within a certain range. In addition, the projected fringe modulation is an important factor: it has a nonlinear negative effect on the phase error, as shown in Wu's experiments [17]. Some researchers have focused their attention on the fringe pitch. Their results have revealed that assuming the pitch is appropriately selected and not below a threshold, a lower value of pitch leads to a smaller phase error [18,19]. Jia et al. observed

---

that if the pitch is divisible by the number of phase-shifting steps, the measurement results are more accurate [10].

Although the above-mentioned factors all improve the measurement accuracy in sinusoidal FPP, the major contributions come from the projected fringe pattern. This is because, no matter how we consider optimizing the FPP system, from Gamma correction, adaptation to BRDF, and carefully selected number of steps and direction of fringe patterns, it is inevitable that an appropriate projection modulation and pitch must be chosen. This paper attempts to optimize the sinusoidal FPP system from these two basic factors. Essentially, they are not independent. We can imagine that for a specific FPP system, it is impractical to capture a fringe pattern with an extremely narrow pitch and high modulation. The constraint is the optical transfer of the projection system. In this work, by analyzing the error model in the FPP and optical projection model, we provide the theoretical proof that there is an optimal projection pitch that yields the peak performance in FPP.

2. FPP system

2.1. Principle of the phase-shifting algorithm

Phase-shifting methods [1] are widely used in FPP because of their high accuracy. In phase-shifting FPP, a series of ideal sinusoidal fringe patterns are generated by a computer and projected onto the measuring surface using a digital projector. The camera observes the reflected fringe pattern from another angle. In this process, we design the projected fringe pattern and capture the observed fringe pattern. There is a nonlinear function between these two fringe patterns, which can be expressed as

$$I_c^i(x, y) = f[I_p^i(x, y)] \tag{1}$$

where $I_p^i(x, y)$ and $I_c^i(x, y)$ are the ith projection and observation fringe of a sequence of N-step ideal sinusoidal fringes, which can be described as

$$I_p^i(x, y) = a_p(x, y) + b_p(x, y)\cos(\Phi + 2\pi i/N_s) \tag{2}$$

and

$$I_c^i(x, y) = a_c(x, y) + b_c(x, y)\cos(\Phi + 2\pi i/N_s) + n(x, y) \tag{3}$$

In Eqs. (2) and (3), $a_p(x, y)$ and $a_c(x, y)$ are the respective backgrounds, whereas $b_p(x, y)$ and $b_c(x, y)$ are the respective modulation functions. In addition, N_s represents the number of phase-shifting steps, generally $N_s \geq 3$; i is an integer, whereas $n(x, y)$ denotes the random noise. The desired phase information Φ can be solved using the following equation, which is explained in [1,20]:

$$\Phi = -\arctan\left(\frac{\sum_{i=0}^{N_s-1} I_c^i(x, y)\sin(2\pi i/N_s)}{\sum_{i=0}^{N_s-1} I_c^i(x, y)\cos(2\pi i/N_s)}\right) = \arctan\left(\frac{b_c \sin\Phi}{b_c \cos\Phi}\right) \tag{4}$$

The phase difference $\Delta\phi(x, y)$ between the reference plane and measuring surface can be found using a phase-shifting algorithm by analyzing the observation frames. Once the phase difference map is obtained, depth information can be recovered from

$$h(x, y) = \frac{l\Delta\phi(x, y)}{2\pi f_0 d} \tag{5}$$

where f_0 is the frequency of the projected fringe pattern. Here d is the length of the baseline, the distance between the two optical centers of camera and projector, and l represents the distance between the camera and the reference plane.

2.2. Error analysis in FPP

In FPP, phase information is demodulated by analyzing the grayscale distribution from observation frames, see Eq. (4). However, phase er-

rors are unavoidable, and usually consist of linear and nonlinear components. For the nonlinear part, a detailed analysis was given in [11], whereas a proof is given in [21] that a FPP system can be approximated as a linear system, when the Gamma of the fringe projector is linearized, the relative height of the measuring surface is much smaller than the working distance, and the amplitudes of the sinusoidal components of the surface are smaller than the linearity surface height limits.

When an FPP system has been corrected to meet the above conditions, the grayscale noise becomes the most significant part of the error source and has a direct effect on the measurement accuracy. In the N-step phase-shifting method, because a multi-frame fringe pattern is adopted, some noise can be offset but not random noise. We assume that random noise $n(x, y)$ obeys the orthodox distribution, and $n(x, y) \in [-N\sqrt{N_s}, N\sqrt{N_s}]$. From Eq. (4), when

$$\Phi + \varphi = \arctan(\frac{b_c \sin(\Phi) + N}{b_c \cos(\Phi) - N}) \tag{6}$$

the phase error φ has the maximum value. Then we have

$$\varphi = \arctan(\frac{b_c \sin(\Phi) + N}{b_c \cos(\Phi) - N}) - \Phi \tag{7}$$

Suppose that $k = \frac{N}{b_c} \in [0, 1)$, then Eq. (7) can be simplified as

$$\varphi = \arctan\left(\frac{\sin(\Phi) + k}{\cos(\Phi) - k}\right) - \Phi \tag{8}$$

Eq. (8) is derived as follows,

$$\frac{d\varphi}{d\Phi} = \frac{1}{1 + \left(\frac{\sin(\Phi)+k}{\cos(\Phi)-k}\right)^2} \frac{\cos(\Phi)(\cos(\Phi) - k) + \sin(\Phi)(\sin(\Phi) + k)}{(\cos(\Phi) - k)^2} - 1$$

$$= \frac{1 + k(\sin(\Phi) - \cos(\Phi))}{(\cos(\Phi) - k)^2 + (\sin(\Phi) + k)^2} - 1 = \frac{1 + k(\sin(\Phi) - \cos(\Phi))}{2k^2 + 1 + 2k(\sin(\Phi) - \cos(\Phi))} - 1 \tag{9}$$

In Eq. (10), assume that

$$y = \sin(\Phi) - \cos(\Phi) = \sqrt{2}\sin(\Phi - \frac{\pi}{4}) \tag{10}$$

owing to $y \in [-\sqrt{2}, \sqrt{2}]$ and $k > 0$, we have

$$2k^2 + 1 + 2k(\sin(\Phi) - \cos(\Phi)) \geq 2k^2 + 1 - 2\sqrt{2}k = (\sqrt{2}k - 1)^2 \geq 0 \tag{11}$$

In Eq. (11), only when $k = \frac{\sqrt{2}}{2}$ and $\Phi = -\frac{\pi}{4}$ do we have $2k^2 + 1 + 2k(\sin(\Phi) - \cos(\Phi)) = 0$. Let $\frac{d\varphi}{d\Phi} = 0$, then when $2k^2 + 1 + 2k(\sin(\Phi) - \cos(\Phi)) \neq 0$, we obtain

$$2k^2 + k(\sin(\Phi) - \cos(\Phi)) = 0 \tag{12}$$

Because $k \neq 0$, we have

$$\sin(\Phi) - \cos(\Phi) = -2k \tag{13}$$

From Eq. (13), we obtain $k \leq \frac{\sqrt{2}}{2}$, and when Φ has the value

$$\Phi_0 = \arcsin\left(-\sqrt{2}k\right) + \frac{\pi}{4} = \arccos\left(\sqrt{2}k\right) - \frac{\pi}{4}$$

Eq. (8) has a maximum value of

$$\varphi_{\max} = \arctan\left(\frac{\sin(\Phi_0) + k}{\cos(\Phi_0) - k}\right) - \Phi_0 = \arcsin\left(\sqrt{2}k\right) \tag{14}$$

where $k = \frac{N}{b_c} \in [0, \frac{\sqrt{2}}{2}]$. If we further substitute $\varphi_{\max}$ into Eq. (5), we obtain

$$\Delta h_{\max} = \frac{l\varphi_{\max}}{2\pi f_0 d} = \frac{l\arcsin\left(\sqrt{2}k\right)}{2\pi f_0 d} = \frac{p\arcsin\left(\sqrt{2}k\right)}{2\pi \tan(\theta)} \tag{15}$$

Here, we define the computing error as

$$Error_{cmpt} = \frac{p \arcsin\left(\sqrt{2}k\right)}{2\pi \tan(\theta)} \qquad (16)$$

and the computing error index (EI) as

$$EI = p \arcsin\left(\sqrt{2}k\right) \qquad (17)$$

2.3. Projecting process for a fringe pattern

In a linear system, when an image $i(x, y)$ is projected onto a screen, each point in the scene is blurred by the optics. Mathematically, the observed image $g(x, y)$ is the result of convolving the corresponding focused image with the optical system's point spread function (PSF) $psf(x, y)$:

$$g(x, y) = psf(x, y) * i(x, y) \qquad (18)$$

The optical PSF is a combination of the diffraction and geometric aberrations [22]. In practice, as an alternative to the preceding PSF model, a two-dimensional Gaussian approximation is often suggested [23]. It is defined as

$$psf(x, y) = \frac{1}{2\pi\sigma^2} \exp\left(-\frac{x^2 + y^2}{2\sigma^2}\right) \qquad (19)$$

In the frequency domain, the Fourier transform of the observed image is the result when the Fourier transform of the object and the optical transfer function (OTF) of the optical system are multiplied:

$$\begin{cases} G(\xi, \eta) = H(\xi, \eta)F(\xi, \eta) \\ H(\xi, \eta) = \exp\left[-\pi^2\sigma^2(\xi^2 + \eta^2)\right] \end{cases} \qquad (20)$$

where $G(\xi, \eta)$ and $F(\xi, \eta)$ are the Fourier transforms of $g(x, y)$ and $i(x, y)$, respectively; $H(\xi, \eta)$ is the OTF, which is also the Fourier transform of the PSF; ξ and η are the spatial frequencies in the x and y direction, respectively. The units of ξ and η are cycles per milliradian (mrad^{-1}).

For a linear FPP system, in the frequency domain, the projection pattern is an impulse response, and the observation pattern is a Gaussian distribution because the ideal sinusoidal fringe pattern is deformed by the measuring surface. In addition, the amplitude of I_c^i will also be weakened because only the direct current component ($f_0 = 0$) can pass without energy loss, which results in a reduction in modulation of the fringe pattern and an increase in measurement error. Fig. 1(a) illustrates how the projected fringe pattern and observed fringe pattern appear in the spatial domain, whereas Fig. 1(b) shows how the OTF affects the projected fringe pattern. If we use a low-frequency fringe pattern, the loss in modulation is definitely lower. However, this also causes a larger measurement error, where Eq. (16) gives the conclusion. Thus, we need to choose the projection frequency carefully to make it optimal.

3. Optimal projection in FPP

3.1. Optical transfer of a pixel array-based projection system

Most digital projectors use a pixel array-based chip to modulate the light source as a projection image, including digital light processing (DLP), liquid crystal display (LCD), and liquid crystal on silicon (LCoS) projectors. According to geometric optics, as shown in Fig. 2, when an object point is not completely focused, the image is blurred. The blurred image of a point on the image detector is circular in shape if the projector has a circular aperture. In that case, it is called the blur circle [22]. We assume that the pixel on the projection chip has the diameter of δ, the diameter of the projection blur circle is $2R'$, which can be found as

$$R' = s\frac{D}{2}\left[\frac{1}{f} - \frac{1}{u} - \frac{1}{s}\right] + \frac{s\delta}{2u} \qquad (21)$$

where u is the distance between the first principal plane and the object plane, and v is the distance between the second principal plane and the
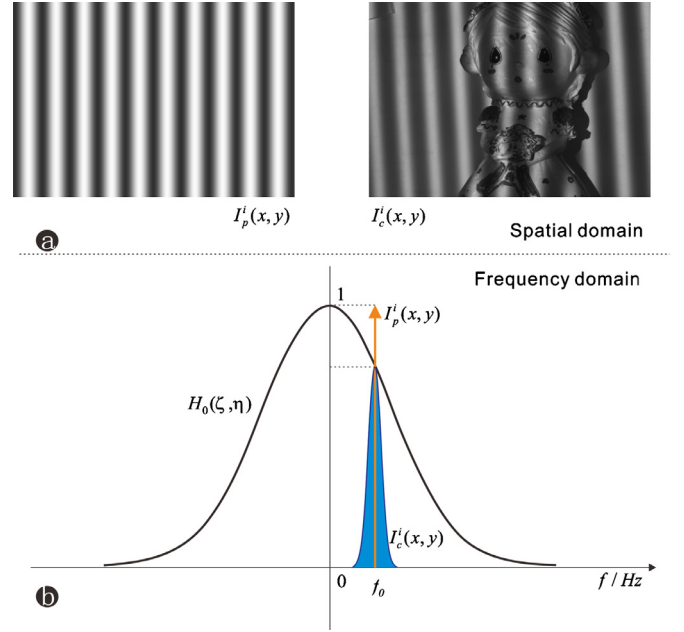

Fig. 1. Projection and observed fringe pattern. (a) Projection and observed fringe pattern in the spatial domain. (b) Projection and observed fringe pattern in the frequency domain.
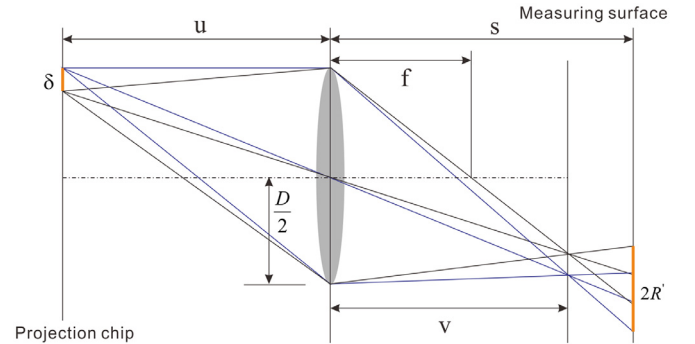

Fig. 2. Projection process for a pixel array-based projector.

image plane. The distance s, focal length f, and aperture diameter D are referred to together as the projector parameters.

For a pixel array-based projector, the PSF and OTF are calculated using Eqs. (19) and (20), where σ is the spread parameter such that $\sigma = cR'$, c is a constant of proportionality ($c > 0$), and c is suggested as $\frac{1}{\sqrt{2}}$ in practice [22]. Replacing $\sigma = cR'$, then we have

$$\sigma_1 = \frac{\sqrt{2}sD}{4}\left[\frac{1}{f} - \frac{1}{u} - \frac{1}{s}\right] + \frac{\sqrt{2}s\delta}{4u} \qquad (22)$$

3.2. Optical transfer of an MEMS scanning projection system

Different from pixel array-based technology, in a micro-electromechanical system (MEMS) scanning FPP system, the fringe pattern is obtained by laser beam scanning instead of pixel array projection [24]. The laser beam in a variety of characteristic patterns or transverse modes that can occur as a pure single mode or, more frequently, as a mixture of several superposed pure modes. The electric field amplitude is described mathematically by a Laguerre–Gaussian function if it has circular symmetry. The simplest mode consists of a single spot with a Gaussian [25],
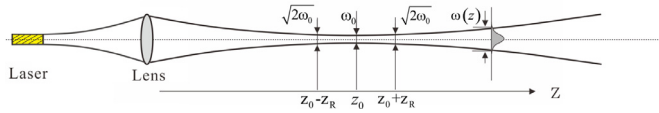
Fig. 3. Propagation characteristic of the laser beam in MEMS projection system. Here ω_0 is the waist diameter and z_R is termed the Rayleigh range.

Fig. 4. Measurement object in our evaluation experiments. (a) Standard 3 mm ceramic gauge block. (b) 3D reconstruction of the standard block using FPP.

as shown in Fig. 3. The actual beam propagation equations describing the change in beam radius $\omega(z)$ with z. Then we have

$$\sigma_2 = \omega(z) = \omega_0 \sqrt{1 + \frac{\lambda^2 (z - z_0)^2}{\pi \omega_0^2}} \qquad (23)$$

In this equation, the minimum beam diameter ω_0 (the waist diameter) is located at z_0 along the propagation axis z. Here λ is the wavelength of the laser. Fig. 3 illustrates the propagation characteristic of the laser beam in the MEMS projection system, where z_R is termed the Rayleigh range.

3.3. Optimization of the FPP system

In Eq. (16), if we take N as a constant variable, then measurement error has a positive correlation with the fringe pitch p, and negative correlation with the observation modulation b_c. Therefore, a fringe pattern with a narrow pitch and high observation modulation delivers high measurement accuracy. However, when the value of p is very low, because b_c has a nonlinear constraint with p and b_p, it is impossible to obtain a high b_c. It is reasonable to consider that there should be an optimal p leading to the best performance in FPP. Section 2.3 shows us the relationship between projected fringe pattern and observed fringe pattern, whereas Sections 3.1 and 3.2 present the detailed optical constraint. From Eq. (20), we have

$$b_c = b_p H_0(\xi, \eta) = b_p \exp \left[-\pi^2 \sigma^2 (\xi^2 + \eta^2) \right] \qquad (24)$$

If we consider the frequency in just one direction, and take the optimal fringe pitch as $p = K/\xi$, replacing b_c with Eq. (24) in Eq. (17), we obtain

$$EI = \frac{K}{\xi} \arcsin \left(\sqrt{2} \frac{N}{b_p \exp \left(-\pi^2 \sigma^2 \xi^2 \right)} \right) \qquad (25)$$

Here, K is a constant variable related to the throw ratio if p takes the unit of pixels; if the unit of p is millimeters, then $K = 1$. For a determined FPP system and measurement distance, K, N, b_p, and σ are constant. Thus, EI is a function of ξ. The derivative of Eq. (25) is

$$\frac{d(EI)}{d\xi} = -\frac{K}{\xi^2} \arcsin \left(\frac{\sqrt{2} N}{b_p} \exp \left(\pi^2 \sigma^2 \xi^2 \right) \right)$$
$$+ \frac{2\sqrt{2} K N \pi^2 \sigma^2}{b_p \sqrt{1 - \frac{2N^2 \exp \left(2\pi^2 \sigma^2 \xi^2 \right)}{b_p^2}}} \exp \left(\pi^2 \sigma^2 \xi^2 \right) \qquad (26)$$

If we set Eq. (26) equal to 0, from the Abel–Rufini theorem [26] we know that this equation has no algebraic solution. However, if given the coefficient we can find a numerical solution, where the EI has a minimum value.

The great significance of this optimization method is that we can obtain the optimal projected fringe pitch by using Eqs. (22) and (26), or Eqs. (23) and (26). Before this, for a given FPP system, we can just find the optimal projection parameters using a series of experiments, which is very time-consuming.

4. Simulations and experiments

In this work, we create an FPP system to verify the proposed optimization theories. A DLP projector with 1280×800 pixels and a mono
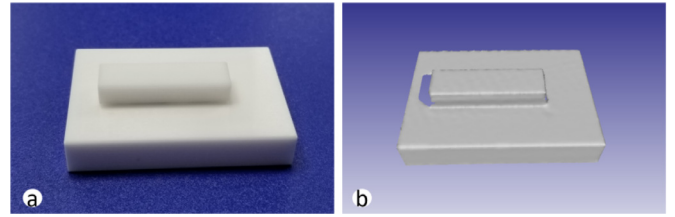
CCD camera with 1920×1200 pixels are used to project and capture the fringe pattern. The baseline between the camera and the projector is 150 mm. A MEMS scanning projector [24] is also employed to evaluate the proposed theories as it has a different projection principle, where the resolution is 1080×720. In this paper, if there is no special explanation, the FPP system is using the DLP projector. To evaluate the performance of proposed methods, a 3 mm standard ceramic gauge block (Fig. 4) with an error of 0.1 μm is employed as a testing object with root-mean-square (RMS) measuring error.

4.1. Simulations and experiments using the FPP error model

In the previous section, we have shown that the maximum error of an FPP system is mainly affected by the pitch and the modulation of fringe patterns, which is denoted by Eq. (16). The simulation results are illustrated in Fig. 5(a), where $p = 5$ mm and $N = 2$, whereas Fig. 5(b) shows the verification experiment results with a 400 mm measurement distance. Furthermore, another experiment, see Fig. 6, shows the relationship between the projected fringe pitch and measurement error, where the captured modulation $b_c = 70$ and the measurement distance $s = 400$ mm. Figs. 5 and 6 verify the error model, where the pitch has a linear effect on the measurement error, whereas the modulation produces a nonlinear effect. Based on the error model, additional experiments are implemented to verify the proposed EI in Eq. (17). Fig. 7 shows an illustration of 25 experiments with different pitches and modulations at a measurement distance of 400 mm, which shows the measurement error has a linear relationship with the EI. Therefore, it is reasonable using the EI as the evaluation for the FPP system.

4.2. Simulation and experiments of optimal projection of an FPP system

We have provided a theoretical basis to demonstrate an optimal pitch for achieving the best performance in FPP, see Eqs. (26) and (25). A simulation is presented to verify the optimization method. In Eq. (25), we set $K = 1$, $N = 5$, $b_p = 75$, and $\sigma = 1$ mm; the simulation result is shown in Fig. 8. When the projection pitch is 4.545 mm, the system has the best performance. A series of experiments are implemented to verify this conclusion. We measured the height of a standard ceramic gauge block with different projection pitches at different measurement distances. Fig. 9(a) shows the results, whereas Fig. 9(b) gives the curve fitting (fifth-degree polynomials) and optimal projection pitch with the measurement distance $s = 400$ mm and $b_p = 70$. Similarly, another series for an MEMS scanning projector was also implemented, see Fig. 10. Owing to the completely different projection principle, it was necessary to perform another experiment on an MEMS scanning projector. In Figs. 9 and 10, these experiments show the FPP system has an optimal projection pitch. In particular, for an MEMS scanning projection FPP system, this optimal value is of greater importance, because when the projected fringe pitch deviates from the optimal value, the measurement error will increase significantly. In Fig. 11, the relationship between the projection pitch and measurement error again verifies the conclusion directly.

The previous content has provided a theoretical proof, simulations, and experiments to demonstrate there is an optimal projection pitch. However, in Eqs. (22) and (23), it is not easy to obtain some of the
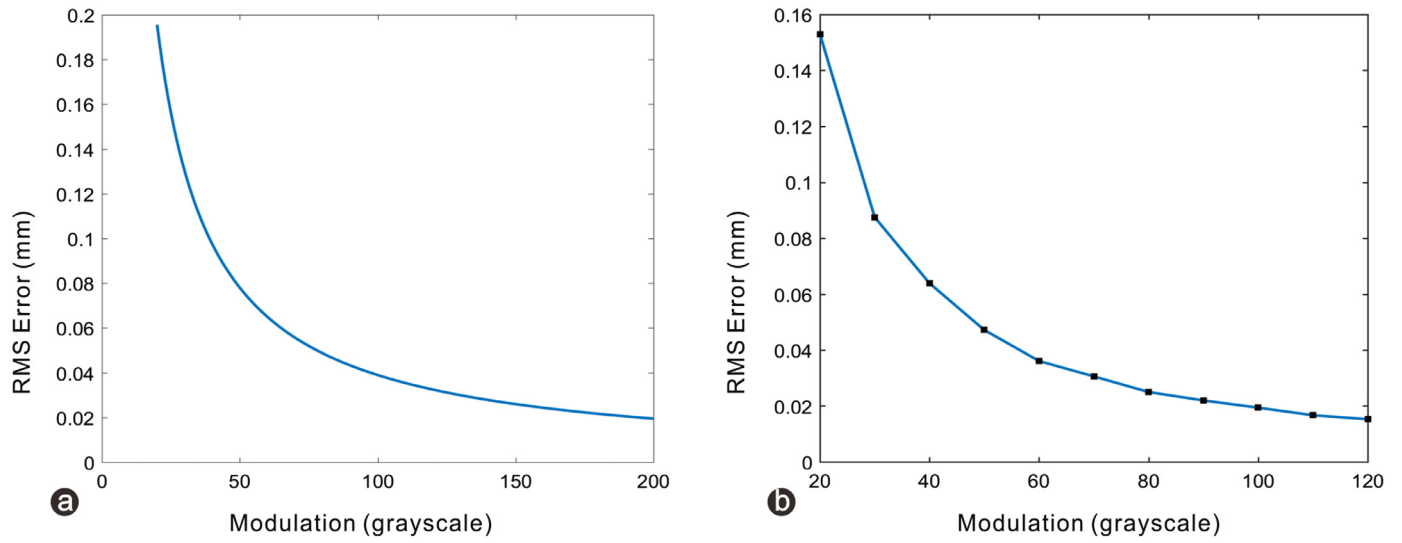
Fig. 5. Relationship between modulation and measurement error. (a) Simulation, captured pitch $p = 5$ mm and captured noise $N = 2$. (b) Experimental data, projection pitch $p_p = 20$ pixels (about 7 mm on the measuring surface).
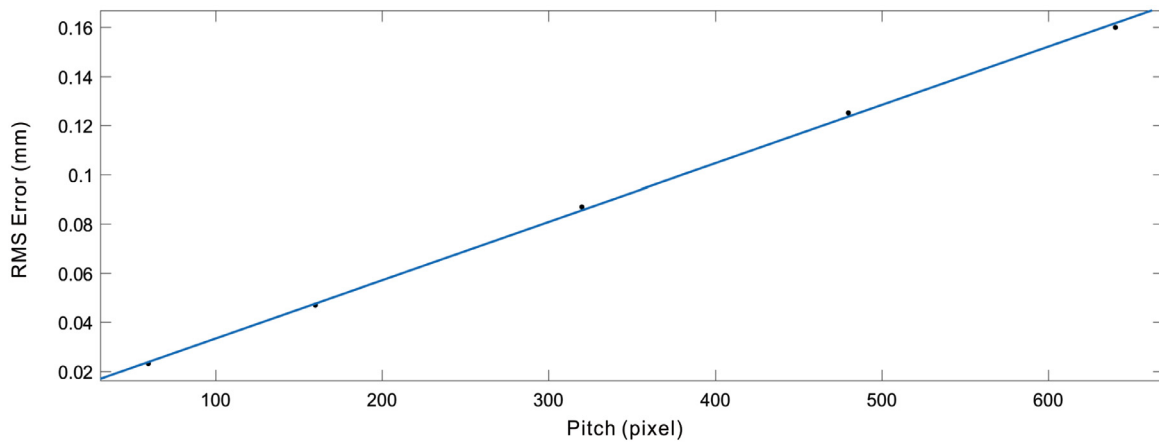

Fig. 6. Relationship between fringe pitch and measurement error, where $b_c = 70$ and measurement distance $s = 400$ mm.
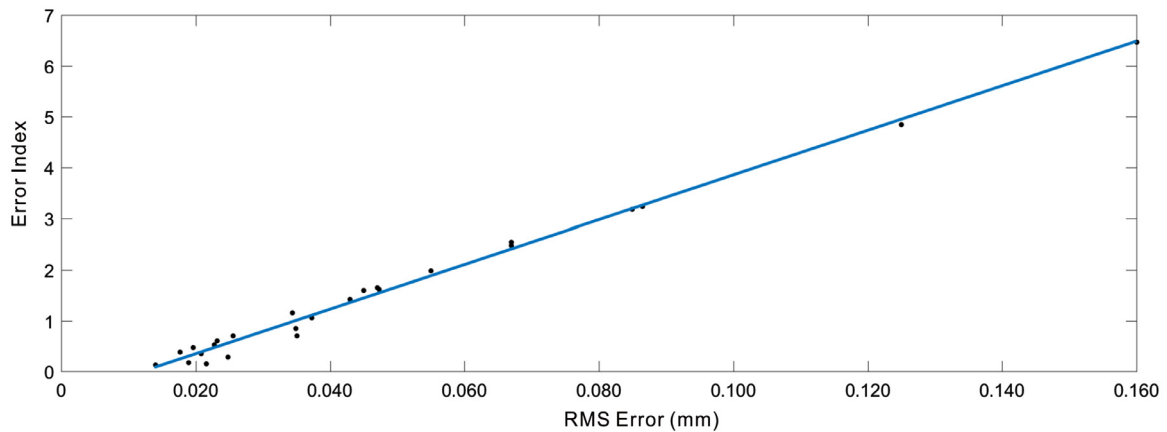

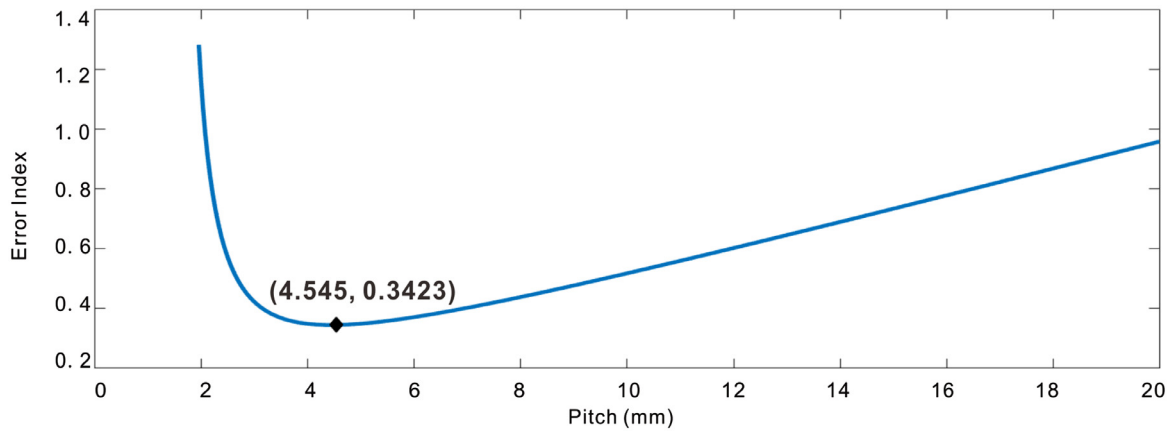**Fig. 7.** Linear fitting of the measurement error and error index.

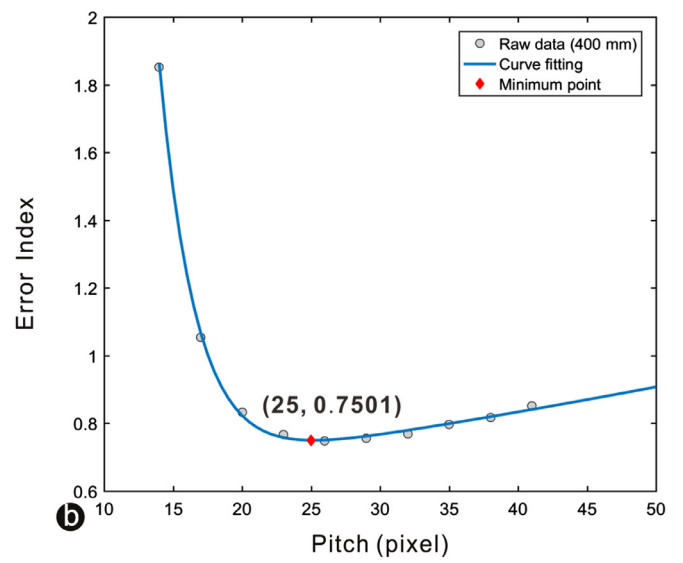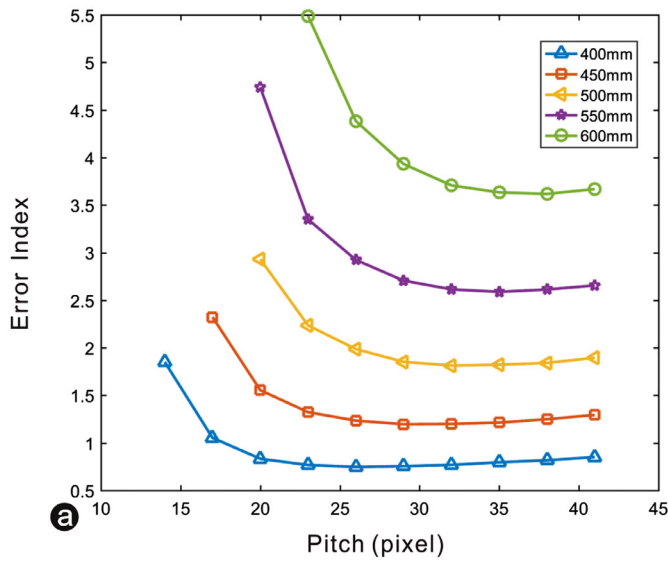Fig. 8. Simulation of the optimal projection pitch.

Fig. 9. Experiments on optimal projection pitch using a DLP projector. (a) Error index changing with projection pitch at different measurement distances. (b) Curve fitting of EI-pitch data with a measurement distance of 400 mm. Here $b_p = 70$.
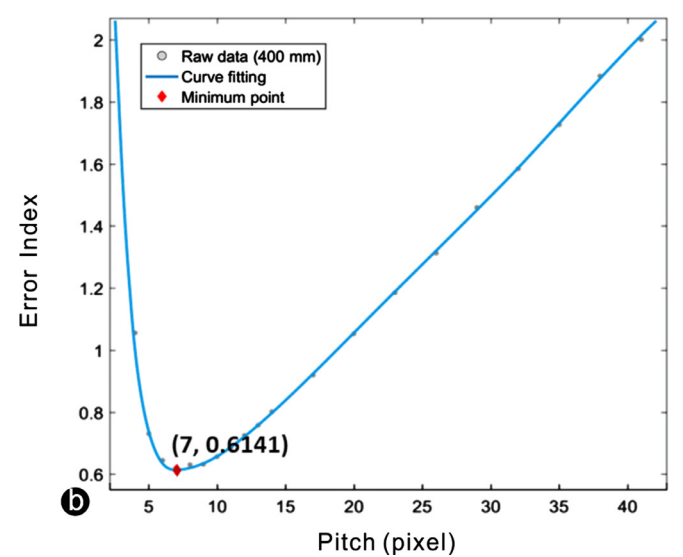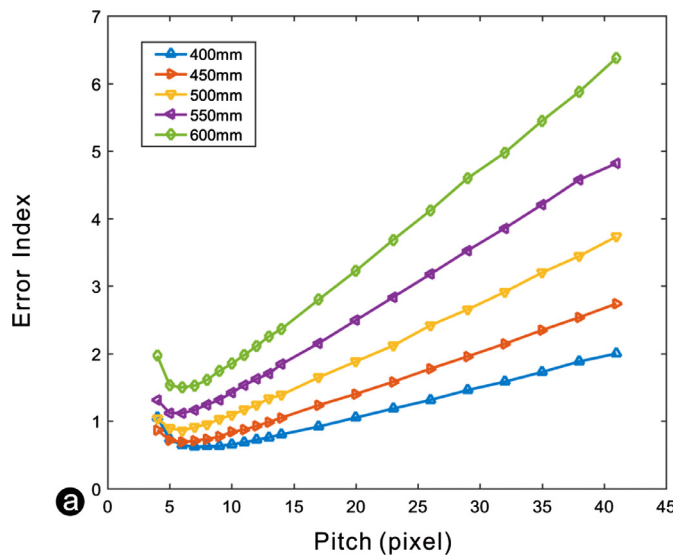

Fig. 10. The experiments on optimal projection pitch with a laser beam MEMS scanning projector FPP system. (a) Error index changing with projection pitch at different measurement distances. (b) Curve fitting of EI-pitch data with a measurement distance of 400 mm. Here $b_p = 70$.
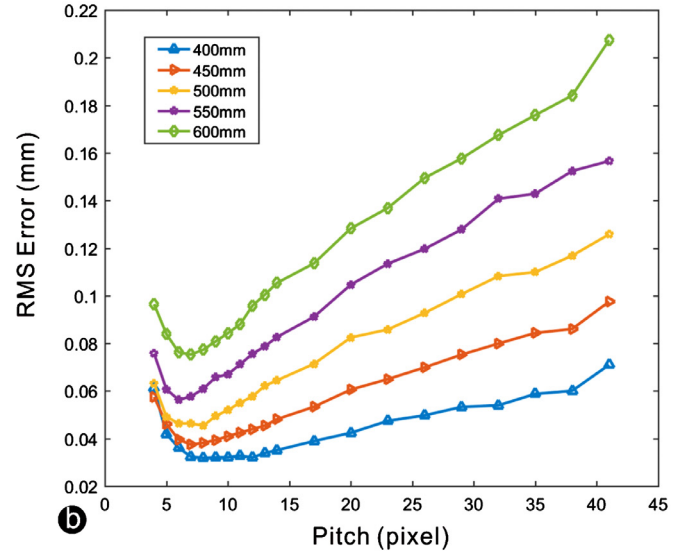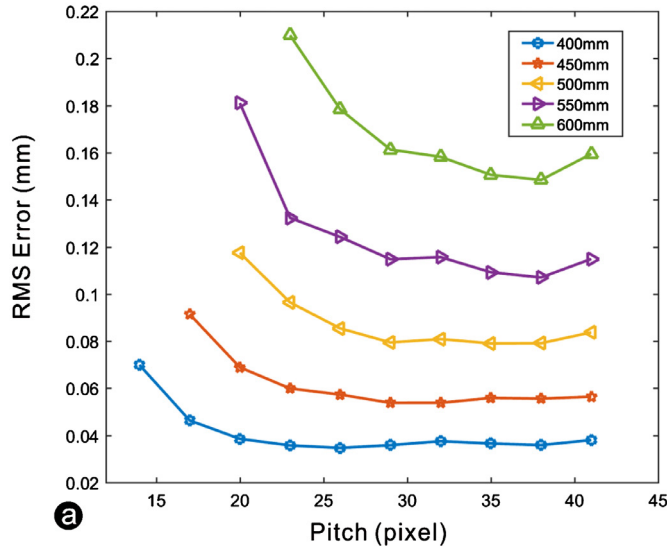
Fig. 11. Relationship between projection pitch and measurement error at different measurement distances. (a) DLP FPP system. (b) Laser beam MEMS scanning projector FPP system. Here $b_p = 70$.

parameters, such as u, f, and ω_0. Here, a simplified method is given to evaluate the optimal projection pitch approximately.

For a pixel array-based projection FPP system, if the projector is well focused and the measuring distance is much larger than height variation of the measuring surface, Eq. (22) can be simplified as

$$\sigma_1 = \frac{\sqrt{2}s\delta}{4u} \tag{27}$$

In fact, the minimum response of the projector is not one physical pixel in the projection chip, but a 2×2 pixel area, which is observed in the experiments with DLP and LCD projectors. In practice, we recommend using

$$\sigma_1 = 2\sqrt{2}\frac{s\delta}{K_{tr}W} \tag{28}$$

where K_{tr} is the throw ratio of the projector (note that the throw ratio varies with the focus distance in pixel array-based projectors), and W is the long side length of the projection chip. A quick example is given here. For the experimental setup, $K_{tr} = 1.158$ with a measuring distance of $s = 400$ mm, $W = 9.855$ mm, and $\delta = 0.01$ mm, so we have $\sigma_1 = 0.9981$ mm. Jointly with Eq. (26), the optimal frequency is solved as $\xi_1 = 0.1591$ Hz, see Appendix A. So the projection pitch with the unit of pixels can be calculated as

$$p_1 = \frac{1280K_{tr}}{s\xi} = 23.29 \text{ pixels} \approx 23 \text{ pixels} \tag{29}$$

which is close to the optimal projection pitch of 25 pixels verified by experiments, as shown in Fig. 9(b).

For an MEMS scanning projector, we still need to find z_0 and ω_0, which can be calculated by using the relationship between the minimum projection point size and measuring distance. In proposed MEMS projection FPP system, $\lambda = 650$ nm, the minimum projection point size with two different distances is measured by using a CCD camera, thus we obtain $P_1(z = 600 \text{ mm}, \omega(z) = 0.35 \text{ mm})$ and $P_2(z = 800 \text{ mm}, \omega(z) = 0.47 \text{ mm})$. Then Eq. (23) is solved, where $z_0 = 498.8$ mm and $\omega_0 = 0.3316$ mm. When $s = 400$ mm, taking Eq. (23) into Eq. (26) and solving this equation (please refer Appendix A), we obtain the optimal frequency of projection pattern $\xi_2 = 0.4491$ Hz. For the MEMS FPP setup, $K_{tr} = 1.2$, then

$$p_2 = \frac{1080K_{tr}}{s\xi} = 7.21 \text{ pixels} \approx 7 \text{ pixels} \tag{30}$$

Fig. 10 (b) provides an illustration that the system achieves the best performance when the projection pitch is 7 pixels with a measuring distance of 400 mm, which meets our optimization results (see Eq. (30)) very well.

5. Conclusion

In this work, we first built an error model for an FPP system. This error model has revealed how the pitch, modulation, and noise of a projected fringe pattern affect the measurement error. Furthermore, the optical transfer has been analyzed to show the constraints between the projection pitch and observation modulation. Combining these components, a theoretical proof has been provided that there is an optimal projection pitch, which yields the best performance for FPP. In addition, an *a priori* optimization method using the common-user accessible parameters has been demonstrated, which can help users to create an optimal FPP system without empirical speculation and time-consuming experiments. Finally, both simulations and experiments have verified the proposed theories. Going forward, we hope our work will be useful when setting up FPP systems.

Appendix A

Here we give an example of how to find the optimal projection frequency ξ when we have σ. Assuming $s = 400$ mm, with Eq. (23) we have

$$\sigma_2 = 0.3316\sqrt{1 + \frac{0.00065^2(z - 498.8)^2}{0.3454}} = 0.3491 \text{ mm} \tag{31}$$

Taking $\sigma_2 = 0.3491$ mm, $K = 1$, $N = 5$, and $b_p = 100$ into Eq. (26), then it can be simplified as

$$\frac{d(EI)}{d\xi} = \frac{2.7915exp(19.739\xi^2)}{\sqrt{1.0 - 0.005exp(39.478\xi^2)}} - \frac{arcsin(0.070711exp(19.739\xi^2))}{\xi^2} \tag{32}$$

For Eq. (32), there is no closed-form solution. Here, we suggest using the Newton iteration to find the numerical solution. The iterative initial

value is set as $\xi_0 = 1$ Hz, and after 8 iterations, we obtain the optimal projection frequency of $\xi_2 = 0.4491$ Hz with an iteration error of 10^{-4}.

Supplementary material

Supplementary material associated with this article can be found, in the online version, at 10.1016/j.optlaseng.2019.07.001.

References

[1] Zuo C, Feng S, Huang L, Tao T, Yin W, Chen Q. Phase shifting algorithms for fringe projection profilometry: a review. Opt Lasers Eng 2018;109:23–59.

[2] Gorthi SS, Rastogi P. Fringe projection techniques: whither we are? Opt Lasers Eng 2010;48(IMAC-REVIEW-2009-001):133–40.

[3] Liu K, Wang Y, Lau DL, Hao Q, Hassebrook LG. Gamma model and its analysis for phase measuring profilometry. JOSA A 2010;27(3):553–62.

[4] Zhang S, Huang PS. Phase error compensation for a 3-d shape measurement system based on the phase-shifting method. Opt Eng 2007;46(6):063601.

[5] Guo H, He H, Chen M. Gamma correction for digital fringe projection profilometry. Appl Opt 2004;43(14):2906–14.

[6] Ma S, Quan C, Zhu R, Chen L, Li B, Tay C. A fast and accurate gamma correction based on fourier spectrum analysis for digital fringe projection profilometry. Opt Commun 2012;285(5):533–8.

[7] Li D, Kofman J. Adaptive fringe-pattern projection for image saturation avoidance in 3d surface-shape measurement. Opt Express 2014;22(8):9887–901.

[8] Lin H, Gao J, Mei Q, He Y, Liu J, Wang X. Adaptive digital fringe projection technique for high dynamic range three-dimensional shape measurement. Opt Express 2016;24(7):7703–18.

[9] Zhang S, Yau S-T. High-resolution, real-time 3d absolute coordinate measurement based on a phase-shifting method. Opt Express 2006;14(7):2644–9.

[10] Jia P, Kofman J, English C. Multiple-step triangular-pattern phase shifting and the influence of number of steps and pitch on measurement accuracy. Appl Opt 2007;46(16):3253–62.

[11] Cai Z, Liu X, Jiang H, He D, Peng X, Huang S, et al. Flexible phase error compensation based on hilbert transform in phase shifting profilometry. Opt Express 2015;23(19):25171–81.

[12] Zhang C, Zhao H, Jiang K. Fringe-period selection for a multifrequency fringe-projection phase unwrapping method. Meas Sci Technol 2016;27(8):085204.

[13] Zhang C, Zhao H, Zhu Q, Zhou C, Qiao J, Zhang L. Phase accuracy evaluation for phase-shifting fringe projection profilometry based on uniform-phase coded image. Meas Sci Technol 2018;29(6):065205.

[14] Lei S, Zhang S. Digital sinusoidal fringe pattern generation: defocusing binary patterns vs focusing sinusoidal patterns. Opt Lasers Eng 2010;48(5):561–9.

[15] Wang Y, Zhang S. Optimal fringe angle selection for digital fringe projection technique. Appl Opt 2013;52(29):7094–8.

[16] Zhang R, Guo H, Asundi AK. Geometric analysis of influence of fringe directions on phase sensitivities in fringe projection profilometry. Appl Opt 2016;55(27):7675–7687.

[17] Wu Y, Yue H, Yi J, Li M, Liu Y. Phase error analysis and reduction in phase measuring deflectometry. Opt Eng 2015;54(6):064103.

[18] Zhang X, Zhu L, Li Y, Tu D. Generic nonsinusoidal fringe model and gamma calibration in phase measuring profilometry. JOSA A 2012;29(6):1047–58.

[19] Dai J, Li B, Zhang S. Intensity-optimized dithering technique for three-dimensional shape measurement with projector defocusing. Opt Lasers Eng 2014;53:79–85.

[20] Pan B, Kemao Q, Huang L, Asundi A. Phase error analysis and compensation for nonsinusoidal waveforms in phase-shifting digital fringe projection profilometry. Opt Lett 2009;34(4):416–18.

[21] Zhang B, Davies A, Evans C, Ziegert J. Validity of the instrument transfer function for fringe projection metrology. Appl Opt 2018;57(11):2795–803.

[22] Subbarao M, Choi T-S, Nikzad A. Focusing techniques. Opt Eng 1993;32(11):2824–37.

[23] Vollmerhausen RH, Reago D, Driggers RG. Analysis and evaluation of sampled imaging systems. SPIE Press Bellingham, Wash, USA; 2010.

[24] Yang T, Zhang G, Li H, Zhou X. Hybrid 3d shape measurement using the mems scanning micromirror. Micromachines 2019;10(1):47.

[25] Marshall GF, Stutz GE. Handbook of optical and laser scanning. CRC Press; 2004.

[26] Żołądek H, et al. The topological proof of Abel-Ruffini theorem. Topol Methods Nonlinear Anal 2000;16(2):253–65.